

# A study on energy resolution of CANDLES detector

B. T. Khai, *Member, IEEE*, S. Ajimura, *Member, IEEE*, W. M. Chan, K. Fushimi, R. Hazama, H. Hiraoka, T. Iida, K. Kanagawa, H. Kino, T. Kishimoto, T. Maeda, K. Nakajima, M. Nomachi, *Senior Member, IEEE*, I. Ogawa, T. Ohata, K. Suzuki, Y. Takemoto, Y. Takihira, Y. Tamagawa, M. Tozawa, M. Tsuzuki, S. Umehara, and S. Yoshida

**Abstract**—In a neutrino-less double-beta-decay ( $0\nu\beta\beta$ ) experiment, an irremovable two-neutrino double-beta-decay ( $2\nu\beta\beta$ ) background surrounds the Q-value of the double beta decay isotope. The energy resolution must be improved to differentiate between  $0\nu\beta\beta$  and  $2\nu\beta\beta$  events. Calcium fluoride for studies of Neutrino and Dark matters by Low Energy Spectrometer (CANDLES) discerns the  $0\nu\beta\beta$  of  $^{48}\text{Ca}$  using a  $\text{CaF}_2$  scintillator as the detector and source. Photomultiplier tubes (PMTs) collect scintillation photons. Ideally, the energy resolution should equal the statistical fluctuation of the number of photoelectrons. At the Q-value of  $^{48}\text{Ca}$ , the current energy resolution (2.6%) exceeds this fluctuation (1.6%). Because of  $\text{CaF}_2$ 's long decay constant of 1000 ns, a signal integration in 4000 ns is used to calculate the energy. The baseline fluctuation ( $\sigma_{\text{baseline}}$ ) is accumulated in the signal integration, degrading the energy resolution. Therefore, this paper studies  $\sigma_{\text{baseline}}$  in the CANDLES detector, which has a severe effect (1%) at the Q-value of  $^{48}\text{Ca}$ . To avoid  $\sigma_{\text{baseline}}$ , photon counting can be used to obtain the number of photoelectrons in each PMT; however, a significant photoelectron signal overlapping probability in each PMT causes missing photoelectrons in counting and reduces the energy resolution. “Partial photon counting” reduces  $\sigma_{\text{baseline}}$  and minimizes photoelectron loss. We thus obtain improved energy resolutions of 4.5–4.0% at 1460.8 keV ( $\gamma$ -ray of  $^{40}\text{K}$ ), and 3.3–2.9% at 2614.5 keV ( $\gamma$ -ray of  $^{208}\text{Tl}$ ). The energy resolution at the Q-value shows an estimated improvement of 2.2%, with improved detector sensitivity by factor 1.09 for the  $0\nu\beta\beta$  half-life of  $^{48}\text{Ca}$ .

**Index Terms**— $\text{CaF}_2$ , photon counting, energy resolution

Manuscript received MM DD, YYYY; accepted MM DD, YYYY. Date of publication: MM DD, YYYY; date of current version, MM DD, YYYY. This work was supported by JSPS/MEXT KAKENHI Grant Number 19H05804, 19H05809, 26104003, 16H00870, 24224007, and 26105513. This work was supported by the research project of Research Center for Nuclear Physics (RCNP), Osaka University. This work was also supported by the joint research program of the Institute of Cosmic Ray Research (ICRR), the University of Tokyo. The Kamioka Mining and Smelting Company has provided service for activities in the mine.

B. T. Khai, W. M. Chan, K. Kanagawa, H. Kino, T. Maeda, T. Ohata, M. Tsuzuki, and S. Yoshida are with the Graduate School of Science, Osaka University, Toyonaka, Osaka 560-0043, Japan.

S. Ajimura, T. Kishimoto, M. Nomachi, Y. Takemoto, Y. Takihira, and S. Umehara are with the Research Center for Nuclear Physics, Osaka University, Ibaraki, Osaka 567-0047, Japan.

K. Fushimi is with the Faculty of Integrated Arts and Science, University of Tokushima, Tokushima 770-8502, Japan.

R. Hazama is with the Faculty of Human Environment, Osaka Sangyo University, Daito, Osaka 574-8530, Japan.

T. Iida is with the Faculty of Pure and Applied Sciences, University of Tsukuba, Ibaraki 305-8571, Japan.

H. Hiraoka, K. Nakajima, I. Ogawa, Y. Tamagawa, and M. Tozawa are with the Graduate School of Engineering, University of Fukui, Fukui 910-8507, Japan.

K. Suzuki is with the Wakasa Wan Energy Research Center, 64-52-1 Nagatani, Tsuruga, Fukui 914-0192, Japan.

## I. INTRODUCTION

### A. Double Beta Decay

DOUBLE beta decay (DBD) is a transition between two isobaric nuclei ( $A, Z$ ) and ( $A, Z + 2$ ) with two decay modes. For two-neutrino DBD ( $2\nu\beta\beta$ ) mode, two electrons and two electron-type anti-neutrinos are emitted. However, an alternative decay mode can occur without anti-neutrino emission, and this is called neutrino-less DBD ( $0\nu\beta\beta$ ). The  $0\nu\beta\beta$  mode is forbidden in the Standard Model of particle physics (SM) due to its violation of lepton number conservation, but it can probe new physics beyond the SM [1]. The discovery of neutrino oscillation indicates that a neutrino has non-zero mass [2], [3]. The remaining questions related to the neutrino mass and whether neutrinos are Majorana or Dirac fermions are attracting the interest of physicists, and the  $0\nu\beta\beta$  experiment is a useful tool for these purposes [1]. The  $2\nu\beta\beta$  mode has been experimentally observed (e.g. the  $2\nu\beta\beta$  half-lives of 10 DBD isotopes are summarized in [4]), but the  $0\nu\beta\beta$  mode has not been observed yet.  $^{48}\text{Ca}$  has the highest DBD Q-value ( $Q_{\beta\beta} = 4272$  keV), but its natural abundance is very low (0.187%). The highest  $Q_{\beta\beta}$  gives a large phase-space factor to enhance the DBD rate and has the least contribution from the natural background.

### B. CANDLES experiment

The Calcium fluoride for studies of Neutrino and Dark matters by Low Energy Spectrometer (CANDLES) experiment aims to obtain  $0\nu\beta\beta$  from  $^{48}\text{Ca}$ . The experiment is very challenging owing to the extremely low decay rate of  $0\nu\beta\beta$  from  $^{48}\text{Ca}$  ( $T_{1/2}^{0\nu} > 5.6 \times 10^{22}$  years with 90% confidence level [5]). To obtain  $0\nu\beta\beta$ , a massive amount of the source and a low background measurement are required. The current CANDLES III experiment is constructed in the Kamioka Underground Observatory (2700 m water equivalent depth) to reduce the cosmic-ray background [6]. We set up an experiment with 96  $\text{CaF}_2$  (un-doped, non-enriched)  $10 \times 10 \times 10$  cm<sup>3</sup> crystals used as both the detector and source. We are developing low-cost enrichment techniques [7], [8], [9] to increase the amount of  $^{48}\text{Ca}$  in our detector in the future. All crystals are submerged inside a 2 m<sup>3</sup> vessel of liquid scintillator (LS). The scintillation decay constants of  $\text{CaF}_2$  and LS are 1000 ns and 10 ns, respectively, and the LS is used as  $4\pi$  active shielding. Scintillation photons are collected by 62 photomultiplier tubes (PMTs) surrounding the vessel, of which 12 are 10-inch (R7081-100), 36 are 13-inch (R8055), and 14 are 20-inch (R7250), all manufactured by Hamamatsu [10]. Light pipes are installed between the LS vessel and PMTs

to increase the efficiency of photon collection. Everything is mounted inside a cylindrical water tank, with a height of 4 m and a diameter of 3 m. To reduce the  $(n, \gamma)$  background in the detector materials and rocks, a passive shield consisting of lead blocks and silicon rubber sheets containing boron carbide ( $B_4C$ ) is installed both inside and outside the tank [11]. More details of the detector setup can be found in [5].

The data acquisition (DAQ) system consists of 74 channels of 500 MHz-8 bits-8 buffers flash analog-to-digital converters (FADCs), of which 62 are recording PMT waveforms and 12 are used for trigger purposes [12]. Trigger logics implemented in the global trigger control of our DAQ system include a dual-gate trigger to select the  $CaF_2$  signal, and other trigger logics for monitoring purposes (a clock trigger of 3 Hz, a minimum bias trigger to select LS signals, a low-threshold dual-gate trigger to select  $CaF_2$  signals at a lower threshold, and a cosmic-ray trigger) [13]. The clock trigger of 3 Hz is used to study single photoelectron charges in dark current and baseline fluctuation, which are discussed in Section II.

### C. $2\nu\beta\beta$ and energy resolution

In  $0\nu\beta\beta$  experiments,  $2\nu\beta\beta$  is an irremovable background proportional to the mass of  $^{48}Ca$ . We plan to develop a ton-scale and highly-enriched- $^{48}Ca$  detector to improve the sensitivity of  $0\nu\beta\beta$  study, so that  $2\nu\beta\beta$  will provide a high-contrast background compared to the  $0\nu\beta\beta$ . The energy distributions of  $2\nu\beta\beta$  and  $0\nu\beta\beta$  of  $^{48}Ca$  are a continuous spectrum and a mono-energetic peak at  $Q_{\beta\beta}$ , respectively. Figure 1 shows simulation energy spectra of  $0\nu\beta\beta$  and  $2\nu\beta\beta$  with different energy resolutions. In this simulation, the  $2\nu\beta\beta$  half-life ( $T_{1/2}^{2\nu}$ ) is  $4.2 \times 10^{19}$  years [4] and  $0\nu\beta\beta$  half-life ( $T_{1/2}^{0\nu}$ ) is assumed to be  $10^{26}$  years, which is equivalent to an effective neutrino mass ( $m_{\beta\beta}$ ) of 80 meV because  $T_{1/2}^{0\nu}$  is proportional to the inverse square of  $m_{\beta\beta}$  [1]. In this simulation,  $m_{\beta\beta}$  is close to the world-best upper limit of  $m_{\beta\beta}$  reported by the Kamioka Liquid-scintillator Anti-Neutrino Detector - Zero neutrino double beta decay search (KamLAND-Zen) [14]. Improving the resolution from 2.6% to 1.6% increases the ratio of  $0\nu\beta\beta$  to  $2\nu\beta\beta$  from 0.2 to 1.0 within the region of interest (ROI); hence, a better energy resolution is required to reduce the  $2\nu\beta\beta$  background.

The  $CaF_2$  signal consists of many photoelectrons (p.e.). In an ideal case, the energy resolution should be equal to the statistical fluctuation of the number of p.e. ( $N_{p.e.}$ ). At the  $Q_{\beta\beta}$  of  $^{48}Ca$ , the current energy resolution of the CANDLES III detector is 2.6% [15] and, with a p.e. yield of 0.91 p.e./keV, the statistical fluctuation of  $N_{p.e.}$  is 1.6%. The resolution is larger than the statistical fluctuation, and other fluctuations are likely to be present that degrade the resolution further. The fluctuations affecting the CANDLES energy resolution include statistical fluctuation, detector stability, crystal position, and charge measurement. Statistical fluctuation is mainly influenced by  $N_{p.e.}$ ; hence, we cool the  $CaF_2$  crystals at approximately 5 °C to increase the scintillation light output, install light pipes to increase the photo-coverage [16], and introduce a magnetic cancellation coil to increase the efficiency of p.e. collection [17]. The detector stability and crystal position were

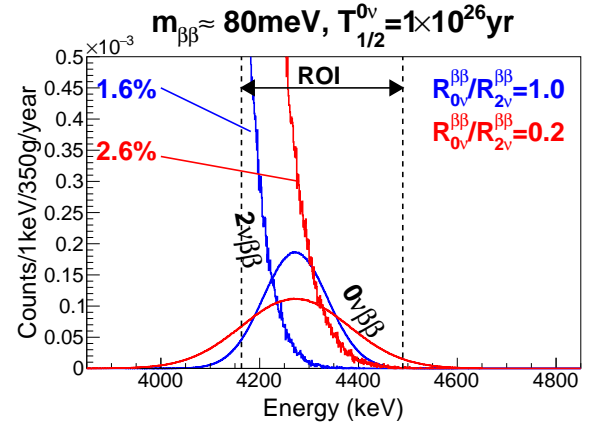


Fig. 1: Simulation histograms of  $0\nu\beta\beta$  and  $2\nu\beta\beta$  of  $^{48}Ca$  with energy resolutions of 2.6% (red) and 1.6% (blue). The ROI to compare the ratio of  $0\nu\beta\beta$  to  $2\nu\beta\beta$  ( $R_{0\nu}^{\beta\beta}/R_{2\nu}^{\beta\beta}$ ) is marked with dashed black lines.

studied in previous research [15], [17], and were found to have a small contribution to the energy resolution of CANDLES. In this paper, the uncertainty in charge measurement of the CANDLES III detector is discussed (Section II), and a method to reduce the uncertainty is introduced (Section III).

## II. ERROR IN CHARGE MEASUREMENT

In the current analysis, we sum the waveforms of 62 PMTs and calculate the charge using signal integration  $= \sum_i (\text{Pedestal} - \text{Signal}[i])$ , where  $i$  is the waveform's time bin, with each time bin equivalent to 2 ns. Because of  $CaF_2$ 's long decay constant of 1000 ns, each signal is integrated in 4000 ns; hence, the baseline fluctuations are accumulated. In this study, we examined possible fluctuations over a long interval, including dark current in the PMTs, noise in the baseline, digitization error (related to the resolution of the FADCs), and pedestal uncertainty. In the following subsections, these long-interval fluctuations at a  $\gamma$ -peak of  $^{40}K$  (1460.8 keV), a  $\gamma$ -peak of  $^{208}Tl$  (2614.5 MeV), and  $Q_{\beta\beta}$  of  $^{48}Ca$  are estimated.

### A. Dark current

Dark current (DC) can be accidentally obtained in a  $CaF_2$  waveform, affecting the energy resolution statistically. For DC analysis, we use the clock trigger events to avoid the p.e. from the scintillator, but the p.e. signals from scintillation photons of low energy radiations may be accidentally collected. To estimate the DC rate in each PMT, a threshold is individually set for each PMT to count the p.e. signals. Details of the threshold setting are described in Section III. Figure 2 shows the DC rates of 62 PMTs, all of which are in the order of  $10^4$  p.e./s. From summing the DC rates of 62 PMTs, the DC rate in the sum waveform is approximately  $\mu_{DC} = 6.2 \times 10^5$  p.e./s. Thus, the DC accumulated in an integration interval  $T_{INT}$  is calculated as  $N_{DC} = \mu_{DC} \times T_{INT}$ , and the fluctuation of DC is  $\sigma_{DC} = \sqrt{N_{DC}}$ . In 4000 ns of the summed waveform, the average amount of DC is 2.5 p.e., and the fluctuation of DC is  $\sigma_{DC} = 1.6$  p.e. The relative uncertainties induced by DC

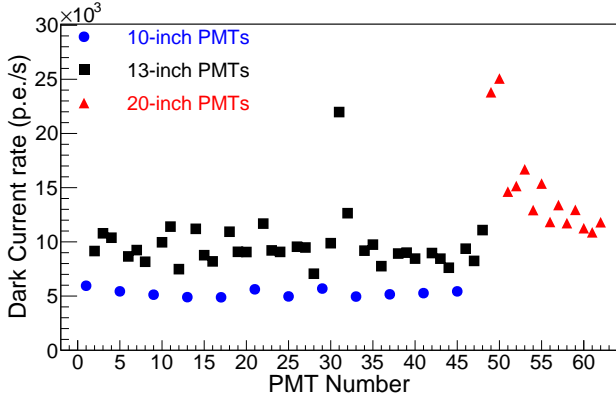


Fig. 2: Dark current rates of 10-inch (12, blue circles), 13-inch (36, black squares), and 20-inch PMTs (14, red triangles).

$(\sigma_{DC}/N_{p.e.})$  at  $^{40}\text{K}$ ,  $^{208}\text{Tl}$ , and  $Q_{\beta\beta}(^{48}\text{Ca})$  are 0.1%, 0.06%, and 0.04%, respectively. The  $N_{p.e.}$  at the  $^{40}\text{K}$  peak,  $^{208}\text{Tl}$  peak, and  $Q_{\beta\beta}(^{48}\text{Ca})$  can be calculated from the p.e. yield.

### B. Noise in baseline

The sine-wave noise of 62 PMTs is analyzed using a clock trigger, with visible noise found in the baseline of the 10-inch PMTs, whereas the noise amplitudes of the 13-inch and 20-inch PMTs are not visible. We sum the 12 baselines of 10-inch PMTs for noise analysis and estimate the effect of noise on the energy resolution. Figure 3 shows a sinusoidal shape of the sum baseline of the 12 10-inch PMTs in one clock event. For every clock event, the sum baseline is fitted with a sine function to estimate the noise amplitude and cycle:

$$A(t) = A_n \sin\left(2\pi \frac{t - \varphi_n}{T_n}\right), \quad (1)$$

where  $A_n$  is the noise amplitude,  $T_n$  is the noise cycle, and  $\varphi_n$  is the phase factor. From analyzing more than  $10^5$  clock events, the mean values of the noise amplitude and cycle are found to be 0.73 ADC, equivalent to approximately 3 mV in the FADC input, and 730 ns, respectively. The noise amplitude is small, although we sum the noise of the 12 10-inch PMTs. Each PMT signal is amplified by 10 times before being fed into an FADC, meaning the noise amplitude is approximately

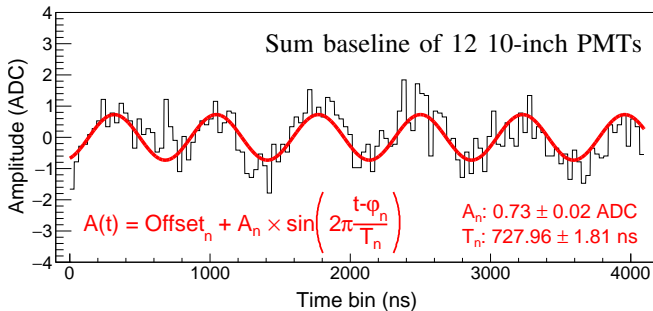


Fig. 3: Sine fitting on the sum baseline of 12 10-inch PMTs in one clock event of CANDLES III.

0.3 mV before amplification. The impedance of each PMT is 50  $\Omega$ ; therefore, the power of the sine-wave noise is only 1.8 nW, which is extremely small. The fluctuation induced by sinusoidal noise in the signal integration in  $T_{INT}$  ns is:

$$\begin{aligned} \sigma_{\text{noise}} &= \int_0^{T_{INT}} A(t) dt \\ &= \frac{A_n T_n}{\pi \bar{\mu}_{p.e.}} \sin\left(\pi \frac{T_{INT}}{T_n}\right) \sin\left(\pi \frac{T_{INT} - 2\varphi_n}{T_n}\right), \end{aligned} \quad (2)$$

where  $\bar{\mu}_{p.e.}$ , which is the average charge of single-p.e. (1 p.e.) signals of the 62 PMTs in the ADC unit, is used to convert  $\sigma_{\text{noise}}$  into p.e. units. The noise effect is clearly a sine function of phase  $\varphi_n$ , which is random in every  $\text{CaF}_2$  event and difficult to estimate. Thus, we estimate the maximum fluctuation induced by the 730-ns-cycle sine noise in this research. The maximum fluctuation, as the root mean square of the sine function in equation 2, is a function of  $T_{INT}$ :

$$\sigma_{\text{noise}}^{\text{max}}(T_{INT}) = \frac{A_n T_n}{\sqrt{2} \pi \bar{\mu}_{p.e.}} \left| \sin\left(\pi \frac{T_{INT}}{T_n}\right) \right|. \quad (3)$$

For the integration interval of 4000 ns, the maximum effect of the 730-ns-cycle noise is 2 p.e.; hence, the maximum relative uncertainties of noise ( $\sigma_{\text{noise}}^{\text{max}}/N_{p.e.}$ ) at  $^{40}\text{K}$ ,  $^{208}\text{Tl}$ , and  $Q_{\beta\beta}(^{48}\text{Ca})$  are 0.15%, 0.08%, and 0.05%, respectively.

### C. Digitization error

We record the PMT waveform using a 500 MHz—8 bits ADC08DL502 from Texas Instruments with 7.5 effective number of bits [18]. The probability of recording a digitized value “n” is the integral within the range  $n \pm 0.5$  of a Gaussian function  $P_n(\mu_A, \sigma_A)$ , where  $\mu_A$  and  $\sigma_A$  are the mean and standard deviation values, respectively, of the analog input. In this study, the pedestal is calculated as the average value of the first 40 data points, equivalent to 80 ns, in the waveform. The measured pedestal, which is theoretically calculated as  $\Sigma_n(n \times P_n)$ . Figure 4 shows the measured pedestal as a function of true pedestal, or  $\mu_A$ , in one PMT. To perform

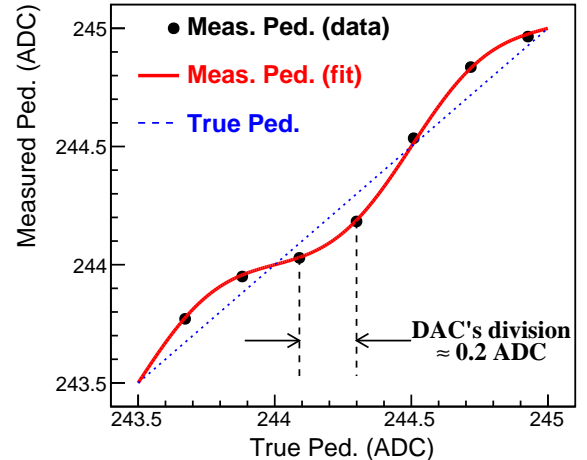


Fig. 4: Measured pedestal plotted as a function of true pedestal with three  $\sigma_A$  values.

the test, we adjust the true pedestal using a 12-bit digital-to-analog converter (DAC), which is installed in each FADC module, with its voltage division equivalent to approximately 0.2 ADC units. The black points depict experimental data obtained at different true pedestal values, the solid red line is the fitting function, and the blue dashed line is the expected true pedestal. Because of the least significant bit (LSB), the measured pedestal is different from the true pedestal, and this difference is called the digitization error (DE). The DE causes a fluctuation in the measured pedestal, which accumulates when calculating the signal integration. In a 1 p.e. signal, the DE accumulates at the non-pedestal points in the width of the 1 p.e. signal. At the pedestal of 244.5 ADC, the DE is zero; thus, the 1 p.e. charge at this pedestal value is not affected by the DE. Because the measured pedestal of each PMT is set at nearly 244.5 ADC, the DE fluctuation on the 1 p.e. charge of one PMT can be assumed to be linearly correlated with the measured pedestal:

$$\Delta_{1 \text{ p.e.}}^{\text{iPMT}} = \text{Slope}^{\text{iPMT}} \times \Delta_{\text{Ped.}}^{\text{iPMT}}, \quad (4)$$

where  $\text{Slope}^{\text{iPMT}}$  is the linear coefficient and  $\Delta_{\text{Ped.}}^{\text{iPMT}}$  is equal to  $\text{Pedestal}^{\text{iPMT}} - 244.5 \text{ ADC}$ . The DE is accumulated at non-pedestal points; if the 1 p.e. signals do not overlap in high- $N_{\text{p.e.}}$  events, the number of non-pedestal points is  $N_{\text{p.e.}}w/\delta$ , where  $w$  is the width of the 1 p.e. signal, and  $\delta$  is the FADC sampling interval (2 ns). In contrast, if many 1 p.e. signals overlap each other, the number of non-pedestal points is reduced. In this study, we estimate the reduction factor using the following mathematical model. The  $\text{CaF}_2$  waveform follows an exponential function:

$$\mu(t) = \mu(0)e^{-t/\tau} = \frac{N_{\text{p.e.}}}{\tau} e^{-t/\tau}, \quad (5)$$

where  $\mu(t)$  is the signal amplitude at time  $t$ , and  $\tau$  is the decay constant of  $\text{CaF}_2$ , which is 1000 ns. The expectation number of p.e. within the width of the 1 p.e. signal is  $\mu(t)w$ , and the probability of obtaining the pedestal point is  $q(t) = e^{-\mu(t)w}$ . The number of non-pedestal points can be deduced as follows:

$$N_{\text{signal}} = \frac{1}{\delta} \int_0^{T_{\text{INT}}} (1 - q(t)) dt, \quad (6)$$

and the reduced factor is estimated as

$$R = \frac{N_{\text{signal}}}{N_{\text{p.e.}}w/\delta}. \quad (7)$$

Each  $\text{CaF}_2$  waveform contains up to several thousands 1 p.e. signals from the 62 PMTs. Because the pedestals and numbers of p.e. are not the same in every PMT, the DE is estimated individually for each PMT using the corresponding  $n_{\text{p.e.}}^{\text{iPMT}}$  and measured pedestal in that PMT:

$$\omega^{\text{iPMT}} = n_{\text{p.e.}}^{\text{iPMT}} \times \Delta_{1 \text{ p.e.}}^{\text{iPMT}} \times R^{\text{iPMT}}, \quad (8)$$

and the DE of the whole detector is the sum of DEs in the 62 PMTs:  $\Omega = \sum_{\text{iPMT}=1}^{62} \omega^{\text{iPMT}}$ . In Figure 5, the distributions of estimated summed DEs of 62 PMTs on the  $\gamma$ -peaks of  $^{40}\text{K}$  and  $^{208}\text{Tl}$  with the Gaussian fitting functions are plotted in blue and red, respectively. The standard deviation of each distribution is due to the fluctuation of the measured pedestal.

For the DE distribution of each energy peak, the mean value of DE ( $\mu_{\text{DE}}$ ) causes a shift in the mean peak, and the standard deviation ( $\sigma_{\text{DE}}$ ) influences the energy resolution. The DE fluctuation depends on the measured pedestal and  $N_{\text{p.e.}}$ , which corresponds to the energy and integration interval. With an integration interval of 4000 ns, the  $\sigma_{\text{DE}}$  at the  $\gamma$ -peaks of  $^{40}\text{K}$  and  $^{208}\text{Tl}$  are 7.3 p.e. and 10.4 p.e., respectively, and the relative fluctuation of DE ( $\sigma_{\text{DE}}/N_{\text{p.e.}}$ ) on these  $\gamma$ -peaks are 0.55% and 0.44%, respectively. According to the obtained fluctuations, the relative fluctuation induced by DE on the  $Q_{\beta\beta}(^{48}\text{Ca})$  should be small.

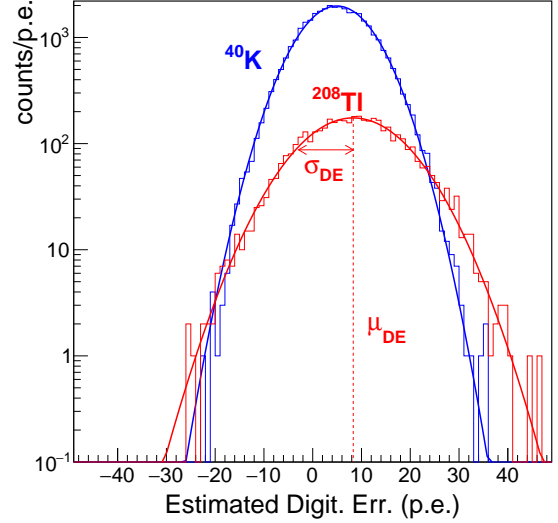


Fig. 5: Distributions of estimated DEs in 62 PMTs with Gaussian fitting at the  $\gamma$ -peaks of  $^{40}\text{K}$  (blue) and  $^{208}\text{Tl}$  (red).

#### D. Pedestal uncertainty

In this study, the pedestal of each PMT is calculated by taking the average of the first 40 sampling points in the waveform. Because the pedestal of each PMT is adjusted to approximately 244.5 ADC, it follows a binomial distribution of 40 trials with the obtained value in each trial either 244 or 245 ADC. Taking  $p$  as the probability of obtaining 245 ADC in a single trial in one PMT, the statistical uncertainty of the pedestal in that PMT is

$$\sigma_{\text{PedStat}}^{\text{iPMT}} = \sqrt{p(1-p)/40}, \quad (9)$$

which is plotted as a solid red line in Figure 6.  $\sigma_{\text{PedStat}}^{\text{iPMT}}$  is the ideal pedestal uncertainty, and the experimental pedestal uncertainty ( $\sigma_{\text{Ped}}^{\text{iPMT}}$ ) in each PMT is obtained by taking the root mean square of the measured pedestal distribution of each PMT. The magenta circles in Figure 6 are the experimental pedestal uncertainties of the 62 PMTs. Because our PMTs are affected by noise,  $\sigma_{\text{Ped}}^{\text{iPMT}}$  is approximately twice as large as  $\sigma_{\text{PedStat}}^{\text{iPMT}}$ . In signal integration, the pedestal uncertainty is accumulated at every data point, and the accumulated fluctuations ( $\sigma_{\text{PedErr}}^{\text{iPMT}}$ ) are linearly proportional to the number of sampling points ( $N$ ):  $\sigma_{\text{PedErr}}^{\text{iPMT}} = N \times \sigma_{\text{Ped}}^{\text{iPMT}}$ . The pedestals of the 62 PMTs are summed in the sum waveform, and the

fluctuation induced by the pedestal uncertainty of the 62 PMTs is amplified by several times:

$$\sigma_{\text{PedErr}} = \sqrt{\sum_{i\text{PMT}=1}^{62} (\sigma_{\text{PedErr}}^{i\text{PMT}})^2}, \quad (10)$$

and  $\sigma_{\text{PedErr}}$  is also linearly proportional to the number of sampling points. In this analysis, we make distributions of integration of the baseline for each PMT, and the root mean square (RMS) of the distribution is  $\sigma_{\text{PedErr}}^{i\text{PMT}}$ . For  $\sigma_{\text{PedErr}}$ , we make the distribution of integration of the sum baseline of the 62 PMTs, and obtain the RMS value.  $\sigma_{\text{PedErr}}$  with the current signal integration calculation can be estimated using an integration interval of 4000 ns (or 2000 sampling points). In the current analysis,  $\sigma_{\text{PedErr}}$  in each 4000 ns integration of the  $\text{CaF}_2$  waveform is 38.6 p.e. The relative fluctuations induced by the pedestal uncertainty of the 62 PMTs, or  $\sigma_{\text{PedErr}}/N_{\text{p.e.}}$ , at the  $^{40}\text{K}$  peak,  $^{208}\text{Tl}$  peak, and  $Q_{\beta\beta}(^{48}\text{Ca})$  are 2.8%, 1.6%, and 1%, respectively.

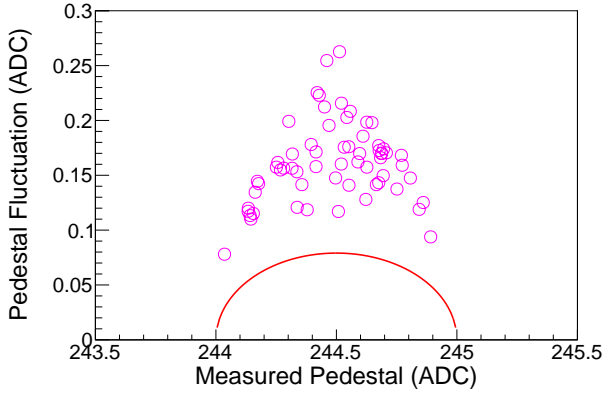


Fig. 6: Standard deviations of measured pedestal distributions plotted with magenta points as a function of measured pedestal of the 62 PMTs. The solid red line is the expected binomial fluctuation.

### E. Summary of baseline fluctuations

The baseline fluctuations are accumulated in the long integration interval of 4000 ns for the  $\text{CaF}_2$  signal and reduce the energy resolution. In this report, we study the baseline fluctuations including DC, sinusoidal noise, DE, and pedestal uncertainty. These fluctuations are plotted as functions of the integration interval, 500–4000 ns, in Figure 7. The DC fluctuation ( $\sigma_{\text{DC}}$ ), which is proportional to  $\sqrt{T_{\text{INT}}}$ , is plotted with a solid blue line. The maximum noise fluctuation ( $\sigma_{\text{noise}}^{\text{max}}$ ), which is calculated using equation 3, is plotted with a solid red line. The estimated DE fluctuations ( $\sigma_{\text{DE}}$ ) as functions of the integration interval at the  $\gamma$ -peaks of  $^{40}\text{K}$  and  $^{208}\text{Tl}$  are plotted with magenta dashed and solid lines, respectively.  $\sigma_{\text{DE}}$  is proportional to  $N_{\text{p.e.}}$ ; therefore, when the integration interval is shrunk,  $N_{\text{p.e.}}$  is reduced, leading to a reduction in  $\sigma_{\text{DE}}$ . Because  $N_{\text{p.e.}}(^{40}\text{K})$  is smaller than  $N_{\text{p.e.}}(^{208}\text{Tl})$ ,  $\sigma_{\text{DE}}(^{40}\text{K})$  is smaller than  $\sigma_{\text{DE}}(^{208}\text{Tl})$ . The fluctuation induced by pedestal uncertainty ( $\sigma_{\text{PedErr}}$ ) in the sum waveform of

the 62 PMTs is calculated with different integration intervals, and plotted as a function of integration interval with a solid black line.  $\sigma_{\text{PedErr}}$  is the most severe, the DE fluctuation is small, and the fluctuations induced by DC and 730-ns-cycle sinusoidal noise are both negligible. The baseline and statistical fluctuations ( $\sigma_{\text{stat}}$ ) at the  $^{40}\text{K}$  peak,  $^{208}\text{Tl}$  peak, and  $Q_{\beta\beta}(^{48}\text{Ca})$  with an integration interval of 4000 ns are listed in Table I. The DE at  $Q_{\beta\beta}$  is not estimated, but the relative DE fluctuation should be small.  $\sigma_{\text{PedErr}}$  is a severe fluctuation compared with  $\sigma_{\text{stat}}$  at  $Q_{\beta\beta}$ . Because  $\sigma_{\text{PedErr}}$  is proportional to the integration interval, the signal integration is poor. An alternative method in CANDLES III is recommended to obtain the energy information with the least effect of baseline fluctuation on the energy.

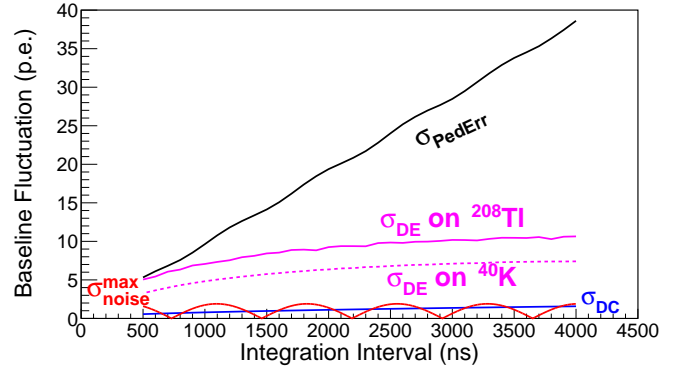


Fig. 7: Baseline fluctuations as a function of integration interval. Fluctuations induced by DC (blue), maximum fluctuation of 730-ns-cycle noise (red), DE at  $\gamma$ -peaks of  $^{40}\text{K}$  (magenta dashed) and  $^{208}\text{Tl}$  (solid magenta), and error in pedestal measurement (black).

TABLE I: All baseline fluctuations ( $\sigma_{\text{DC}}$ ,  $\sigma_{\text{noise}}$ ,  $\sigma_{\text{DE}}$ , and  $\sigma_{\text{PedErr}}$ ) and statistical fluctuation ( $\sigma_{\text{stat}}$ ) at the  $^{40}\text{K}$  peak,  $^{208}\text{Tl}$  peak, and  $Q_{\beta\beta}(^{48}\text{Ca})$  with an integration interval of 4000 ns.

	$^{40}\text{K}$ $\gamma$ -peak 1460.8 keV	$^{208}\text{Tl}$ $\gamma$ -peak 2614.5 keV	$Q_{\beta\beta}(^{48}\text{Ca})$ 4272 keV
$\sigma_{\text{DC}}$	1.6 p.e.	1.6 p.e.	1.6 p.e.
( $\sigma_{\text{DC}}/N_{\text{p.e.}}$ )	(0.1%)	(0.06%)	(0.04%)
$\sigma_{\text{noise}}$	$\leq 2$ p.e.	$\leq 2$ p.e.	$\leq 2$ p.e.
( $\sigma_{\text{noise}}/N_{\text{p.e.}}$ )	( $\leq 0.15\%$ )	( $\leq 0.08\%$ )	( $\leq 0.05\%$ )
$\sigma_{\text{DE}}$	7.3 p.e.	10.41 p.e.	
( $\sigma_{\text{DE}}/N_{\text{p.e.}}$ )	(0.6%)	(0.4%)	(small)
$\sigma_{\text{PedErr}}$	38.6 p.e.	38.6 p.e.	38.6 p.e.
( $\sigma_{\text{PedErr}}/N_{\text{p.e.}}$ )	(2.9%)	(1.6%)	(1.0%)
$\sigma_{\text{stat}} = \sqrt{N_{\text{p.e.}}}$	36.5 p.e.	48.8 p.e.	62.3 p.e.
( $\sigma_{\text{stat}}/N_{\text{p.e.}}$ )	(2.7%)	(2.0%)	(1.6%)

## III. PHOTON COUNTING IN CANDLES III

### A. DAQ for photon counting

The unavoidable fluctuation induced by the pedestal uncertainty is accumulated in the signal integration. The photon counting method is widely used in scintillator experiments to reduce baseline fluctuations. The sum waveform of the  $\text{CaF}_2$  signal is formed by up to several thousands of p.e. signals,



and each PMT waveform contains less  $N_{\text{p.e.}}$ . The overlap of 1 p.e. signals results in inefficiency in photon counting, as mentioned in III-B; hence, we should count  $N_{\text{p.e.}}$  in each PMT of CANDLES. Currently, the first 768 ns of each PMT waveform is digitized by an FADC every 2 ns and recorded as 8-bit data; thereafter, digitized values in every 64 ns is summed and recorded as 16-bit data [12]. The waveform interval of each FADC is 8960 ns, and the data size is 640 B/FADC/event [12]. The 1 p.e. width of each PMT is less than 50 ns; thus, the shape of the 1 p.e. signal is difficult to see if the signal rises after 768 ns. The DAQ software is modified to record the first 4088 ns of the waveform at a speed of 2 ns/sample, and records 128 ns by summing the digitized values for every 64 ns. After DAQ modification, the waveform interval is reduced to 4216 ns, and the data size is increased to 2048 B/FADC/event, which is the limit of buffer size in each FADC. Using data from a previous study [12], the readout time per event for photon counting measurement is 20 ms/event, which is twice as long as the current readout time in the physics run of CANDLES [12]. Owing to the development of the DAQ with eight buffers acting as derandomizers [12] in each FADC, the data-taking efficiency with the increased data size is still almost 100%.

### B. Overlap of single p.e. signals

The threshold for photon counting should not be set too low to avoid baseline noise, or too high to avoid losing p.e. in counting. In this study, the threshold for each PMT is  $\text{Pedestal} - (\mu_p - 2\sigma_p)$ , where  $\mu_p$  and  $\sigma_p$  are the mean and standard deviation, respectively, of 1 p.e. pulse height distribution of the corresponding PMT. This threshold is set for every PMT because it provides a good separation between the baseline and non-baseline signals. For every time bin in 4088 ns of the waveform, if the signal crosses over the threshold, it is counted as 1 p.e. With simple photon counting, a multi-p.e. signal is counted as a single p.e. signal, which leads to missing p.e. in counting.

If the time interval between the two 1 p.e. signals is too short, it is impossible to distinguish them in photon counting. We use a simple mathematical model to estimate the number of counted p.e. from the number of true p.e. We assume that there are two adjacent 1 p.e. signals in one PMT, named “A” and “B”, respectively, and thus define signal interval ( $w_s$ ) as the shortest interval to distinguish these two signals. The  $w_s$  value is related to the 1 p.e. signal width of the PMT. To avoid missing signal B in counting, there should be no signal in the  $w_s$  ns preceding signal A. The probability of counting signal B is the probability of no signal in the  $w_s$  ns preceding signal A:  $e^{-\mu(t)w_s}$ , where  $\mu(t)$  is defined in equation 5. The number of counted p.e. ( $N_c$ ) is

$$\begin{aligned} dN_c &= \mu(t)e^{-\mu(t)w_s} dt \\ \Rightarrow N_c &= \int_0^\infty dN_c = \frac{\tau}{w_s} \left(1 - e^{-N_{\text{p.e.}}w_s/\tau}\right). \end{aligned} \quad (11)$$

The counting efficiency in a PMT is evaluated in Figure 8 by checking the correlation of the counted p.e. and the signal integration. The green dashed line indicates the expected 100%

counting efficiency, and the solid red line is the fitting function using equation 11. At  $Q_{\beta\beta}(^{48}\text{Ca})$ , the number of p.e. is approximately 63 p.e./PMT, whereas the number of counted p.e. in this PMT is approximately 40 p.e. Two histograms constructed using signal integration in 4000 ns and photon counting in 4000 ns are plotted in black and magenta, respectively, in Figure 9. It is very clear that the histogram using 4000 ns photon counting has a worse energy resolution due to missing many p.e. in counting.

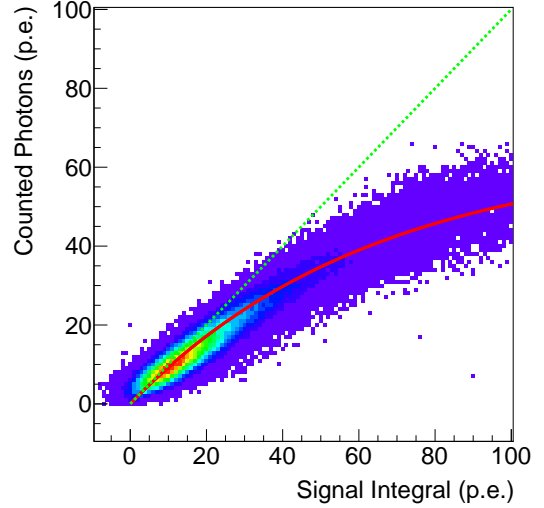


Fig. 8: Counting efficiency in a PMT. The green dashed line is the expected linearity, and the solid red line is the fitting function.

### C. Partial photon counting

The severe baseline fluctuations are accumulated in the 4000 ns integration interval (Section II); therefore, it is encouraged to use photon counting instead of signal integration in CANDLES III. However, the spectrum constructed using 4000 ns photon counting has a poor energy resolution (Section III) because the overlap of 1 p.e. signals leads to missing p.e. in counting. In this section, we introduce a method named “partial photon counting” (PPC) to reduce the baseline fluctuation with the fewest possible missed p.e. in photon counting. The multi-p.e. signals are found predominantly near the rising edge of the  $\text{CaF}_2$  waveform. Thus, each PMT waveform is divided into two regions: in the prompt region near the rising edge, where many multi-p.e. signals are found, signal integration is used to avoid missing p.e.; and in the latter region near the tail, where only a few multi-p.e. signals are found, photon counting is performed to reduce the baseline fluctuation. The sum of the integration and photon-counting intervals is fixed at 4000 ns. From summing the waveforms of 62 PMTs, we can get the energy of  $\text{CaF}_2$  signal. The details of the PPC method for the CANDLES detector and some preliminary results of improved energy resolutions obtained with a Gaussian-plus-exponential fitting function are introduced in reference [19]. Energy histograms are constructed with different mixtures of integration and photon-counting intervals to evaluate the performance of PPC. Several histograms

constructed using the PPC method are shown in Figure 9 with different mixtures including 4000 ns (integration), 3000 ns (integration) + 1000 ns (counting), 2000 ns (integration) + 2000 ns (counting), 1000 ns (integration) + 3000 ns (counting), and 4000 ns (counting), plotted in black, red, green, blue, and magenta, respectively. Because the counting efficiency is not 100%, the energy peaks are left-shifted when the photon-counting interval is increased. Therefore, all energy histograms in Figure 9 are calibrated using  $\gamma$ -peaks of  $^{40}\text{K}$  and  $^{208}\text{Tl}$  in this research for ease of further analysis.

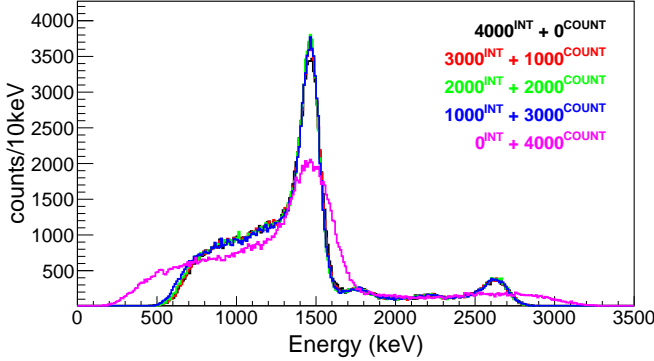


Fig. 9: Energy histograms constructed using the PPC method after calibration. Histograms using different mixtures of integration and photon-counting intervals are shown.

Each energy histogram obtained in PPC is fitted with a function, which is a sum of Gaussian functions, including the  $\gamma$ -peaks emitted from  $^{40}\text{K}$  (1.46 MeV [20]),  $^{214}\text{Bi}$  (1.76 MeV and 2.2 MeV [20]), and  $^{208}\text{Tl}$  (2.6 MeV [20]), and an error function, as the Compton and other background. Figure 10 shows the energy spectrum constructed with a 4000 ns integration interval with the fitting function. The energy resolutions at  $^{40}\text{K}$  and  $^{208}\text{Tl}$  peaks in each histogram are checked. To evaluate the performance of the PPC method, the resolutions are plotted as a function of the integration interval in Figure 11. The estimated resolutions at the  $^{40}\text{K}$  and  $^{208}\text{Tl}$  peaks are

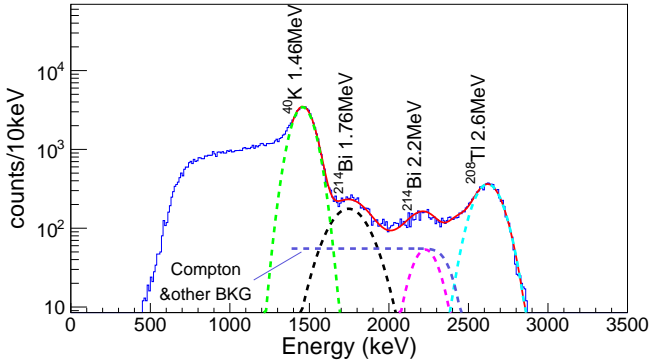


Fig. 10: Fitting function (solid red line) applied to every energy spectrum to obtain the energy resolutions of the  $^{40}\text{K}$  and  $^{208}\text{Tl}$  peaks. The fitting function contains Gaussian peaks ( $\gamma$ -peaks of  $^{208}\text{Tl}$ ,  $^{214}\text{Bi}$ , and  $^{40}\text{K}$ ) and an error function as the Compton and other background.

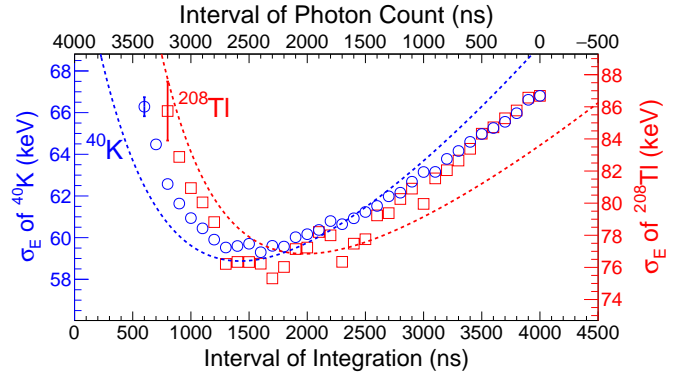


Fig. 11: Obtained energy resolution at  $^{40}\text{K}$  (blue circles) and  $^{208}\text{Tl}$  (red squares) peaks as a function of integration interval. The estimated resolutions at the  $^{40}\text{K}$  and  $^{208}\text{Tl}$  peaks are plotted with blue and red dashed lines, respectively. The lines are plotted using equation 15.

plotted using blue and red dashed lines, respectively. The estimated resolutions are calculated using equation 15, which is the root sum square of all fluctuations examined in this study. The differences between the experimental and estimated values at both energy peaks may be caused by imperfect estimation of the statistical fluctuation, which is discussed in the next paragraph, and the assumption of remaining fluctuation, which is discussed in IV-A. The differences between the experimental and estimated values are small (less than 4 keV) at both energy peaks. For each  $\gamma$ -peak, the errors of adjacent data points are correlated; therefore, only one error bar at one integration interval is shown. Owing to the small number of events at the  $^{208}\text{Tl}$  peak, we found deviation of the obtained resolutions at this energy peak as well as a wide error bar. The energy resolutions at the two energies are improved owing to the reduction of baseline fluctuation when the integration interval is decreased. Near the rising edge, the energy resolutions degrade because more p.e. are missed, due to the high overlapping probability of 1 p.e. signals. Because there are more p.e. obtained at the  $^{208}\text{Tl}$  peak compared to the  $^{40}\text{K}$  peak, the overlapping probability of 1 p.e. signals at the  $^{208}\text{Tl}$  peak is higher compared to that at the  $^{40}\text{K}$  peak. The integration interval to obtain the best energy resolution at the  $^{208}\text{Tl}$  peak should be longer than that at the  $^{40}\text{K}$  peak to limit the p.e. missed in counting. From the results, we obtain the energy deviation ( $\sigma_E$ ) improved from 66.8 to 59.3 keV, or energy resolution ( $\sigma_E/E$ ) improved from 4.5% to 4.0%, at the  $^{40}\text{K}$  peak when reducing the integration interval from 4000 to 1600 ns; and  $\sigma_E$  improved from 86.7 to 75.3 keV, or  $\sigma_E/E$  improved from 3.3% to 2.9% at the  $^{208}\text{Tl}$  peak when reducing the integration interval from 4000 to 1700 ns. With the results at the  $^{40}\text{K}$  and  $^{208}\text{Tl}$  peaks, it is expected to obtain an improved resolution at  $Q_{\beta\beta}(^{48}\text{Ca})$ .

The overlap of 1 p.e. signals degrades the energy resolution because of the increment in the statistical fluctuation. The statistical fluctuation in PPC is estimated using the following mathematical model. The regions in PPC include the prompt region for integration and the latter region for photon counting.

With the predefined parameters in equation 5, the number of p.e. in the prompt region ( $N_P$ ) is

$$N_P = \int_0^{T_{\text{INT}}} \mu(t) dt = N_{\text{p.e.}} (1 - e^{-t/\tau}). \quad (12)$$

The number of p.e. in the latter region is  $N_D = N_{\text{p.e.}} e^{-t/\tau}$ , and the number of counted p.e. in the latter region of a PMT waveform,  $M_D$ , is calculated using equation 11:

$$M_D = \frac{\tau}{w_s} (1 - e^{-N_D w_s / \tau}). \quad (13)$$

The obtained number of p.e. ( $N_T$ ) is the sum of  $N_P$  and  $M_D$ . Because  $N_T$  is normalized to  $N_{\text{p.e.}}$  in the analysis, the statistical fluctuation after calibration is

$$\Delta N_T = \sqrt{\Delta N_P^2 + \Delta M_D^2 \left( \frac{dN_D}{dM_D} \right)^2}. \quad (14)$$

Applying equation 14 with different mixtures of integration and photon-counting intervals, the statistical fluctuations in the PPC method at the  $^{40}\text{K}$  and  $^{208}\text{Tl}$  peaks are estimated. The statistical fluctuations at these two peaks are plotted as functions of the integration interval with the two solid black lines in Figure 12.

#### IV. RESULTS AND DISCUSSION

##### A. Discussion of the fluctuations

In Figure 12, we summarize the fluctuations at the  $^{40}\text{K}$  and  $^{208}\text{Tl}$   $\gamma$ -peaks, and plot them as a function of integration interval. The statistical fluctuations estimated by equation 14 are shown as solid black lines. Extending the photon-counting interval increases the number of 1 p.e. signals overlapping each other; hence, those p.e. are missed in counting, and the statistical fluctuation becomes worse. The root sum squares of the statistical and baseline fluctuations,  $\sqrt{\sigma_{\text{stat}}^2 + \sigma_{\text{baseline}}^2}$ , at the two energy peaks are plotted as solid red lines. The baseline fluctuations include the pedestal uncertainty,  $\sigma_{\text{PedErr}}$ , and the DE,  $\sigma_{\text{DE}}$ . Because the fluctuations induced by DC,  $\sigma_{\text{DC}}$ , and sinusoidal noise,  $\sigma_{\text{noise}}$ , are negligibly small, they are not accounted for in the baseline fluctuations. Additionally, photon counting cannot remove the DC 1 p.e. signals in the  $\text{CaF}_2$  waveform, so the DC fluctuation cannot be reduced by the PPC method. In addition to the baseline fluctuation and estimated statistical fluctuation, we study the remaining fluctuation as a function of integration interval. The remaining fluctuations,  $\sigma_{\text{Remain}} = \sqrt{\sigma_E^2 - \sigma_{\text{baseline}}^2 - \sigma_{\text{stat}}^2}$ , of the two energy peaks are plotted as magenta points. The remaining fluctuation at the  $^{208}\text{Tl}$  peak is almost unchanged for  $T_{\text{INT}}$  of 600–4000 ns. At the  $^{40}\text{K}$  peak, we obtain some uncertainties of remaining fluctuation at  $T_{\text{INT}} > 3000$  ns or  $T_{\text{INT}} < 1500$  ns. The statistical fluctuation is estimated imperfectly with a simple mathematical model (to calculate the overlap of 1 p.e. signals), which leads to uncertainties in the remaining fluctuation at the  $^{40}\text{K}$  peak. In general, the remaining fluctuation can be assumed to be independent of the integration interval, and its source is not determined in this study.

Because the remaining fluctuation can be assumed to be independent of the integration interval, the tendency of improved resolution by the PPC method can be explained by

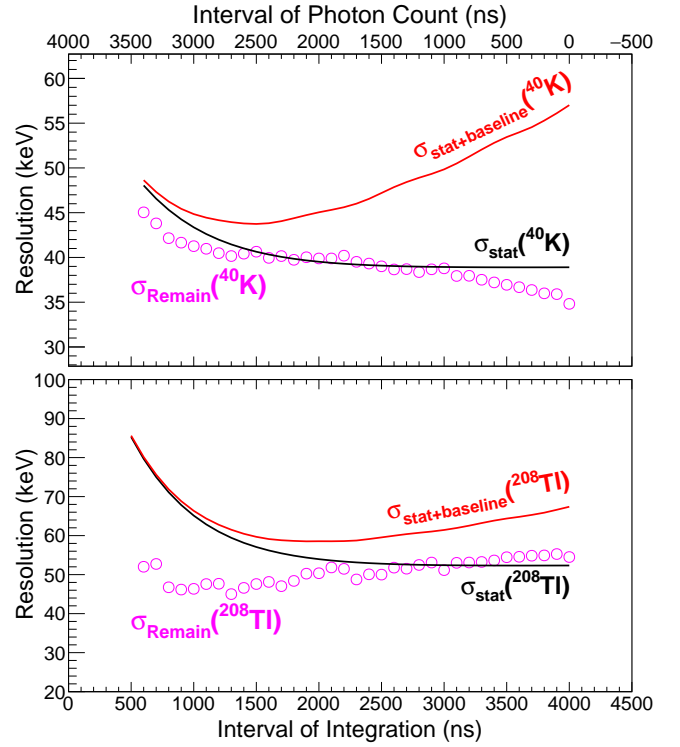


Fig. 12: The statistical fluctuations, statistical+baseline fluctuations, and remaining fluctuations at  $^{40}\text{K}$  and  $^{208}\text{Tl}$   $\gamma$ -peaks are plotted as a function of the integration interval.

the reduction of baseline fluctuation. In Figure 12, for each energy peak, the average value of remaining fluctuation is close to the statistical fluctuation at a 4000 ns integration interval. Assuming that the remaining fluctuation is zero with no incident p.e., the function  $\text{Remain}(E) = a \times \sqrt{E}$  can explain the remaining fluctuations at 0 keV, 1460 keV ( $^{40}\text{K}$ ), and 2614 keV ( $^{208}\text{Tl}$ ). By fitting the remaining fluctuations at the  $^{40}\text{K}$  and  $^{208}\text{Tl}$  peaks in all the PPC histograms, the obtained parameters  $a$  fluctuate around 1. Using this function for each combination of integration and photon-counting intervals allows the remaining fluctuation at  $Q_{\beta\beta}(^{48}\text{Ca})$  to be extrapolated from the remaining fluctuations at the  $^{40}\text{K}$  and  $^{208}\text{Tl}$  peaks. Figure 13 shows the remaining fluctuations at the  $^{40}\text{K}$  peak,  $^{208}\text{Tl}$  peak, and  $Q_{\beta\beta}(^{48}\text{Ca})$ . The remaining fluctuation at each energy is the average of all remaining fluctuations obtained with a 600–4000 ns integration interval, and its error bar is the standard deviation. The function  $y = \sqrt{E}$ , plotted with a solid line, can explain the dependence of the remaining fluctuation on the energy.

In summary, the energy resolution can be calculated using the following function:

$$\sigma_E = \sqrt{\sigma_{\text{stat}}^2 + \sigma_{\text{DE}}^2 + \sigma_{\text{Remain}}^2 + \sigma_{\text{PedErr}}^2}, \quad (15)$$

where  $\sigma_{\text{stat}}$  is the statistical fluctuation,  $\sigma_{\text{DE}}$  is the DE fluctuation,  $\sigma_{\text{Remain}}$  is the remaining fluctuation, and  $\sigma_{\text{PedErr}}$  is the accumulated fluctuation induced by pedestal uncertainty. The estimated DE corresponds to  $N_{\text{p.e.}}$ , so the  $\sigma_{\text{DE}}$  fluctuation depends on  $\sqrt{E}$ . From the above discussion,



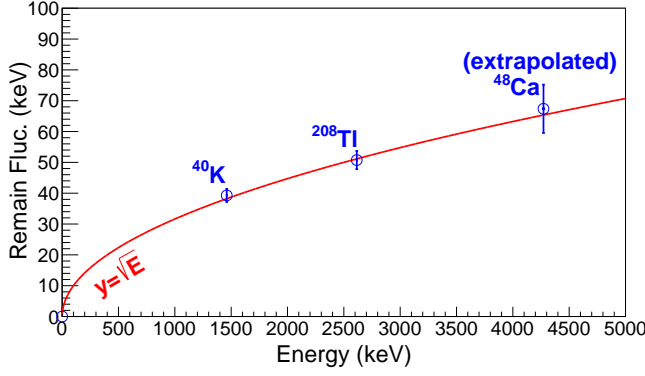


Fig. 13: Remaining fluctuation as a function of energy. The circles represent the remaining fluctuations at  $\gamma$ -peaks of  $^{40}\text{K}$  and  $^{208}\text{Tl}$ , and at the Q-value of  $^{48}\text{Ca}$ . The remaining fluctuation at the Q-value is estimated assuming  $\text{Remain}(E) = a \times \sqrt{E}$ , where  $a$  fluctuates around 1.0, so  $y = \sqrt{E}$  is plotted in this figure.

the fluctuations studied in this research can be categorized into two groups: energy-dependent fluctuations ( $\sigma_{\text{stat}}$ ,  $\sigma_{\text{DE}}$ , and  $\sigma_{\text{Remain}}$ ), which are proportional to  $\sqrt{E}$ , and energy-independent fluctuation ( $\sigma_{\text{PedErr}}$ ). We assume that the energy resolution can be estimated by the following fitting function:

$$\frac{\sigma_E}{E} = \sqrt{\frac{p_0}{E^2} + \frac{p_1}{E}}. \quad (16)$$

The goodness of the above fitting function is evaluated by applying it to the energy resolutions taken from [21] obtained at different energies. In Figure 14, the energy peaks consist of  $\gamma$ -peaks from radioisotopes ( $^{40}\text{K}$ ,  $^{208}\text{Tl}$ , and  $^{88}\text{Y}$ ), and  $\gamma$ -peaks from  $(n, \gamma)$  reactions on  $^1\text{H}$ ,  $^{28}\text{Si}$ ,  $^{56}\text{Fe}$ , and  $^{58}\text{Ni}$ . The details of  $(n, \gamma)$  calibration for the CANDLES III detector and the emitted  $\gamma$ -peaks can be found in [21].

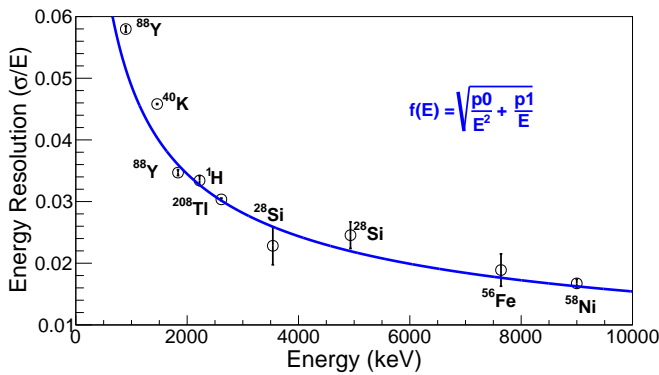


Fig. 14: Application of the fitting function in equation 16 on the obtained resolutions in Run010 of CANDLES. The data points are referred from [21].

### B. Estimating the improved sensitivity of CANDLES III

For each mixture of integration and photon-counting intervals, equation 16 is used to fit the energy resolutions at the  $^{40}\text{K}$  and  $^{208}\text{Tl}$  peaks. The energy resolution at  $Q_{\beta\beta}(^{48}\text{Ca})$  is then

extrapolated. The estimated results are plotted as a function of integration interval with blue circles in Figure 15. The uncertainty of the blue circles at the 1200–2600 ns integration interval, shown in Figure 15, is due to the uncertainty of the resolutions obtained at the  $^{40}\text{K}$  and  $^{208}\text{Tl}$  peaks plotted in Figure 11. The energy resolutions at  $Q_{\beta\beta}(^{48}\text{Ca})$  reported by Ohata [15] and Iida [21] are obtained with the 4000 ns integration method, and plotted with black triangles and red squares, respectively. With an integration interval of 4000 ns, there is an agreement between the estimated resolution at  $Q_{\beta\beta}(^{48}\text{Ca})$  in this study and those obtained in previous studies. From the figure, the energy resolution at  $Q_{\beta\beta}(^{48}\text{Ca})$  can be improved from 2.6% to 2.2% by using the PPC method when the integration interval is reduced from 4000 to 2300 ns.

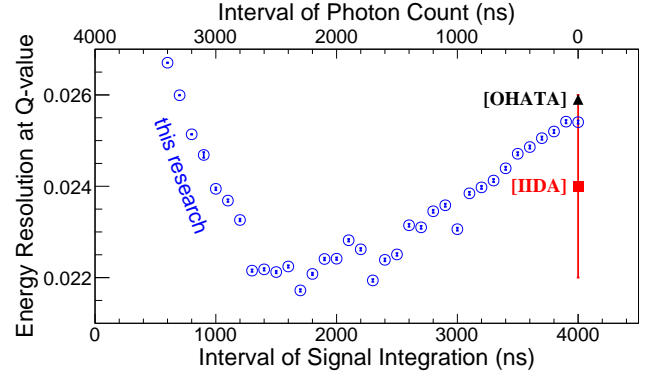


Fig. 15: Estimated energy resolutions at the Q-value using the PPC method. The blue circles represent the  $\sigma_E(Q_{\beta\beta})$  estimated in this study. The black triangle and red square indicate the  $\sigma_E(Q_{\beta\beta})$  obtained in previous studies by Ohata [15] and Iida [21], respectively.

The sensitivity of  $T_{1/2}^{0\nu}$  is related to the background rate and energy resolution. In the current CANDLES III, the  $2\nu\beta\beta$  background is not dominant compared to the natural background, and the sensitivity of  $T_{1/2}^{0\nu}$  is proportional to the inverse square root of the energy resolution at  $Q_{\beta\beta}$  [1]. The energy resolution at  $Q_{\beta\beta}(^{48}\text{Ca})$  is estimated to be improved from 2.6%, by using a 4000 ns integration, to approximately 2.2%, by using PPC. Therefore, using the PPC method can improve the sensitivity of the CANDLES III detector for  $T_{1/2}^{0\nu}$  of  $^{48}\text{Ca}$  by  $\sqrt{2.6\%/2.2\%} = 1.09$  times.

## V. SUMMARY

CANDLES aims to obtain the  $0\nu\beta\beta$  of  $^{48}\text{Ca}$  using  $\text{CaF}_2$  crystals. The  $2\nu\beta\beta$  mode is an irremovable background in CANDLES, and it can be a high-contrast background in our future ton-scale detector with  $\text{CaF}_2$  (un-doped,  $^{48}\text{Ca}$ -enriched) crystals. To reduce the  $2\nu\beta\beta$ , it is necessary to improve the energy resolution. At  $Q_{\beta\beta}(^{48}\text{Ca})$ , the energy resolution, 2.6%, is larger than the ideal statistical fluctuation of the number of p.e., 1.6%, and there are other fluctuations that worsen the energy resolution. The baseline fluctuations are accumulated in the 4000 ns signal integration, which is used to calculate the energy of  $\text{CaF}_2$ . In this study, the baseline fluctuations are investigated, and the fluctuation induced by

pedestal uncertainty is found to be the most severe fluctuation of 1% at  $Q_{\beta\beta}(^{48}\text{Ca})$ . Photon counting is useful for removing the baseline fluctuations, but it results in missing p.e. in counting for each PMT and, consequently, a worse energy resolution. We introduce a method named “partial photon counting”, in which the signal integration is carried out in the prompt region and the photon counting is carried out in the tail region, to improve the energy resolution. Using this method, we obtain an improvement in the energy resolutions at  $\gamma$ -peaks of  $^{40}\text{K}$  and  $^{208}\text{Tl}$ , and the energy resolution at  $Q_{\beta\beta}$  is estimated to be improved to 2.2%. With this improvement, we expect the sensitivity of  $T_{1/2}^{0\nu}$  of  $^{48}\text{Ca}$  to be improved by 1.09 times using the same detector status as that reported in [15].

## VI. ACKNOWLEDGMENT

The authors thank Mr. Keita Mizukoshi from Kobe University for his helpful discussions and comments.

## REFERENCES

- [1] M. J. Dolinski *et al.*, “Neutrinoless Double-Beta Decay: Status and Prospects,” *Annu. Rev. Part. Sci.*, vol. 69, no. 1, pp. 219–251, 2019. DOI: 10.1146/annurev-nucl-101918-023407.
- [2] S. Fukuda *et al.* (Super-Kamiokande Collaboration), “Solar  $^8\text{B}$  and hep Neutrino Measurements from 1258 Days of Super-Kamiokande Data,” *Phys. Rev. Lett.*, vol. 86, pp. 5651–5655, 2001. DOI: 10.1103/PhysRevLett.86.5651.
- [3] Q. R. Ahmad *et al.* (SNO Collaboration), “Direct Evidence for Neutrino Flavor Transformation from Neutral-Current Interactions in the Sudbury Neutrino Observatory,” *Phys. Rev. Lett.*, vol. 89, p. 011301, 2002. DOI: 10.1103/PhysRevLett.89.011301.
- [4] A. Barabash, “Average (Recommended) Half-Life Values for Two-Neutrino Double-Beta Decay,” *Czechoslovak Journal of Physics*, vol. 52, no. 4, pp. 567–573, 2002. DOI: 10.1023/A:1015369612904.
- [5] S. Ajimura *et al.* (CANDLES Collaboration), “Low background measurement in CANDLES-III for studying the neutrino-less double beta decay of  $^{48}\text{Ca}$ ,” arXiv:2008.09288 [hep-ex], 2020.
- [6] Y. Suzuki *et al.*, “Kamioka Underground Observatories,” *The Eur. Phys. J. Plus*, vol. 127, no. 9, p. 111, 2012. DOI: 10.1140/epjp/i2012-12111-2.
- [7] T. Kishimoto *et al.*, “Calcium isotope enrichment by means of multi-channel counter-current electrophoresis for the study of particle and nuclear physics,” *Prog. Theor. Exp. Phys.*, vol. 2015, no. 3, 2015. DOI: 10.1093/ptep/ptv020.
- [8] S. Umehara *et al.*, “A basic study on the production of enriched isotope  $^{48}\text{Ca}$  by using crown-ether resin,” *Prog. Theor. Exp. Phys.*, vol. 2015, no. 5, 2015. DOI: 10.1093/ptep/ptv063.
- [9] K. Matsuoka *et al.*, “The laser Isotope separation (LIS) methods for the enrichment of  $^{48}\text{Ca}$ ,” in *The 16th International Conference on Topics in Astroparticle and Underground Physics (TAUP 2019)*, vol. 1468, p. 012199, IOP Publishing, 2020. DOI: 10.1088/1742-6596/1468/1/012199.
- [10] Hamamatsu K. K., “Photomultiplier Tubes”. [Online] Available: [https://www.hamamatsu.com/resources/pdf/etd/LARGE\\_AREA\\_PMT\\_TPMH1376E.pdf](https://www.hamamatsu.com/resources/pdf/etd/LARGE_AREA_PMT_TPMH1376E.pdf) (R7081), <https://www.alldatasheet.com/datasheet-pdf/pdf/397638/HAMAMATSU/R7250.html> (R8055 and R7250).
- [11] K. Nakajima *et al.*, “Performance of updated shielding system in CANDLES,” in *The 6th International Workshop on Low Radioactivity Techniques (LRT 2017)*, vol. 1921, p. 060003, 2018. DOI: 10.1063/1.5018999.
- [12] B. T. Khai *et al.*, “ $\mu\text{TCA}$  DAQ system and parallel reading in CANDLES experiment,” *IEEE Trans. Nucl. Sci.*, vol. 66, no. 7, pp. 1174 – 1181, 2019. DOI:10.1109/TNS.2019.2900984.
- [13] T. Maeda *et al.*, “The CANDLES Trigger System for the Study of Double Beta Decay of  $^{48}\text{Ca}$ ,” *IEEE Trans. Nucl. Sci.*, vol. 62, no. 3, pp. 1128–1134, 2015. DOI: 10.1109/TNS.2015.2423275.
- [14] A. Gando *et al.* (KamLAND-Zen Collaboration), “Search for Majorana Neutrinos Near the Inverted Mass Hierarchy Region with KamLAND-Zen,” *Phys. Rev. Lett.*, vol. 117, p. 082503, 2016. DOI: 10.1103/PhysRevLett.117.082503.
- [15] T. Ohata, “Search for Neutrinoless Double Beta Decay in  $^{48}\text{Ca}$  with the CANDLES III experiment,” Doctor Thesis, Osaka University, section 4.2, p. 42, 2018. DOI: 10.18910/69325.
- [16] S. Umehara *et al.*, “CANDLES - Search for neutrino-less double beta decay of  $^{48}\text{Ca}$ ,” in *The International Nuclear Physics Conference (INPC) 2013*, vol. 66, p. 08008, 2014. DOI: 10.1051/epjconf/20146608008.
- [17] T. Iida *et al.*, “Status and future prospect of  $^{48}\text{Ca}$  double beta decay search in CANDLES,” in *The 16th International Conference on Topics in Astroparticle and Underground Physics (TAUP 2015)*, vol. 718, p. 062026, 2016. DOI: 10.1088/1742-6596/718/6/062026.
- [18] Texas Instrument Inc., “Adc08dl502 datasheet.” [Online]. Available: <http://www.ti.com/lit/ds/symlink/adc08dl502.pdf>.
- [19] B. T. Khai *et al.*, “Photon counting method for improvement of energy resolution in CANDLES experiment,” in *2019 IEEE Nuclear Science Symposium and Medical Imaging Conference (NSS/MIC)*, pp. 1–4, 2019. DOI: 10.1109/NSS/MIC42101.2019.9059670.
- [20] Japan Atomic Energy Agency, “Nuclear data center.” [Online]. Available: <https://www.ndc.jaea.go.jp/NuCl/>.
- [21] T. Iida *et al.*, “The energy calibration system for CANDLES using  $(n,\gamma)$  reaction,” arXiv:2003.13404 [physics.ins-det], 2020.